DESIGN AND SIMULATION ANALYSIS OF AN INTEGRATED XYZ MICRO-ACTUATOR FOR CONTROLLING DISPLACEMENT OF A SCANNING PROBE

VAN HIEU DANG

Hanoi University of Science and Technology, International Training Institute for Materials Science, Hanoi, Vietnam, and FPT University, Hanoi, Vietnam

VAN TAM LE

Hanoi University of Science and Technology, International Training Institute for Materials Science, Hanoi, Vietnam

KAZUHIRO HANE

Tohoku University, Department of Finemechanics, Sendai, Japan

MANH HOANG CHU

Hanoi University of Science and Technology, International Training Institute for Materials Science, Hanoi, Vietnam
e-mail: hoangcm@itims.edu.vn; hoang.chumanh@hust.edu.vn

We report an integrated micro-actuator for independent control of the displacement in three orthogonal directions. Electrostatic comb drives are employed for controlling the displacement in the x and y directions while a parallel plate-type actuation is used for driving the displacement in the z direction. The three actuators are mechanically coupled, but are electrically isolated. The calculation models are established for investigating the operation characteristics of the micro-actuator. The calculated results are in good agreement with those obtained by the finite element method in Comsol Multiphysics 4.3. The results of modal analysis show that the displacement in the three orthogonal directions can be independently controlled with low mode cross-talk.

Keywords: integrated xyz micro-actuator, mode cross-talk, mechanical coupling bridge, electrical isolation trench

1. Introduction

Recently, micro-actuators are of great interest for a variety of applications such as in nanopositioning, oscillating performance, mechanical sensors and scanning probe lithography (Liu *et al.*, 2007; Legtenberg *et al.*, 1996; Sasaki *et al.*, 2008; Huo *et al.*, 2010; Hu *et al.*, 2017). Micro--actuators can be one-, two- or multi-dimensional (Liu *et al.*, 2007; Legtenberg *et al.*, 1996; Sasaki *et al.*, 2008). To drive a structure in a certain direction, a micro-actuator has to be constructed from springs, which is compliant to that motion direction. To drive a micro-actuator in one dimension in plane or out-of-plane, folded beam springs are often used because they can supply stable operation with large displacement (Liu *et al.*, 2007; Legtenberg *et al.*, 1996). For an xy two-dimensional micro-actuator, one often employs springs used in one-dimensional micro--actuator and arranges them in two x and y orthogonal directions (Sasaki *et al.*, 2008). There are also designs of xyz three-dimensional micro-actuators reported in literature (Liu *et al.*, 2007; Correa *et al.*, 2016; Ando, 2004; Dong and Ferreira, 2009; Kim *et al.*, 2014; Takahashi *et al.*, 2009). In (Correa *et al.*, 2016; Ando, 2004; Dong, 2009; Kim *et al.*, 2014), springs for the xyz actuation are connected softly together or directly connected to the center plate without stiff gimbal frames, so the cross-axis coupling of motion still exists. An algorithm for compensating

the coupled motion error was proposed in (Kim *et al.*, 2014). To drive the xyz actuator independently, topological configuration using electrical isolation trenches, stiction bars as an electrical jump wire, and mechanical coupling deploying stiff gimbal frames were introduced in (Takahashi *et al.*, 2009). In this work, bidirectional lateral comb drives are used for the x- and y-motions using flexural springs, whereas a unidirectional vertical comb drive is used for the z-motion using the torsion spring. To drive the xyz micro-actuator, one can use actuation mechanisms such as piezoelectric, thermal or electrostatic actuation (Liu *et al.*, 2007; Legtenberg *et al.*, 1996; Sasaki *et al.*, 2008; Correa *et al.*, 2016; Ando, 2004; Dong, 2009; Kim *et al.*, 2014; Takahashi *et al.*, 2009; Xu *et al.*, 2006; Wang *et al.*, 2004). In these actuation mechanisms, electrostatic actuation is preferred for operation with low power consumption due to capacitance-based actuation without current. On the other hand, much effort is made to improve mechanical structures for sensing applications with high precision (Trinh *et al.*, 2013; Weinberg and Kourepenis, 2006; Acar and Shkel, 2009), however, there are no many reports on the xyz micro-actuator that has a mechanically decoupled structure for easy and precise control of the displacements. Moreover, a xyz micro-actuator having the capability of independent control of the displacements and an easy fabrication process is necessary to report for applications in high precise positioning, low-noise sensing, and scanning probe lithography.

Therefore, we report here a xyz micro-actuator whose its displacements in three orthogonal directions can be independently controlled. The operation characteristics of the micro-actuator are analytically investigated by solid and fluidic mechanical theory and electrostatic theory. The calculated results are also compared to those obtained by the finite element method.

2. Design of xyz micro-actuator

The concept of the proposed xyz micro-actuator is shown in Fig. 1a. The micro-actuator is constructed of two components, an xy actuator consisting of electrostatic comb drives, comb drives 1 and 2 for controlling the x-axis displacement, comb drives 3 and 4 for controlling the y-axis displacement, and a parallel-plate electrostatic actuator (z-axis actuator) for controlling the out-of-plane (z-axis) displacement (Figs. 1b and 1c). The center plate can be independetly drived in the x and y axes by the xy actuator. This is obtained by designing springs, which is compliant to one motion direction. These springs are then orthogonally designed which respond to displacements along the x and y axes. In this work, we employ folded beam springs, see Fig. 1d, which supplies stable operation with large displacements (Legtenberg *et al.*, 1996). The z-axis actuator consists of a center plate that is suspended by extended crab-leg beam springs, Fig. 1c. The comb drives are mechanically coupled, but isolated electrically by separated gaps using insulation bridges, Fig. 1e, (Chu *et al.*, 2011). The comb drives are designed on the fixed and movable suspending frames. In this work, we propose to directly integrate the counter electrode at the backside of the center plate to form a parrallel-plate capacitive actuator which can be fabricated by the silicon-on-insulator technology on a single chip. This will reduce effort in fabricating xyz micro-actuators using a complicated assembly process as reported in (Liu *et al.*, 2007). To supply a potential to the counter electrode, we use the contact hole as shown in Fig. 1f.

To drive the xyz micro-actuator under DC voltage, we can establish a common ground line for the comb drives and the plate electrode using a folded beam spring of the x-axis actuator. The remaining electrodes use three remaining folded beam springs of the x-axis actuator for supplying voltages. However, to dynamically drive the xyz actuator, more electric interconnection lines are required. To effectively use the actuation of both sides of the xy actuator, three electrodes are required for each axis, x or y (Chu *et al.*, 2011). Therefore, we propose an xyz micro-actuator with folded beam springs modified in Fig. 2, in which the four folded springs in Fig. 1 devided
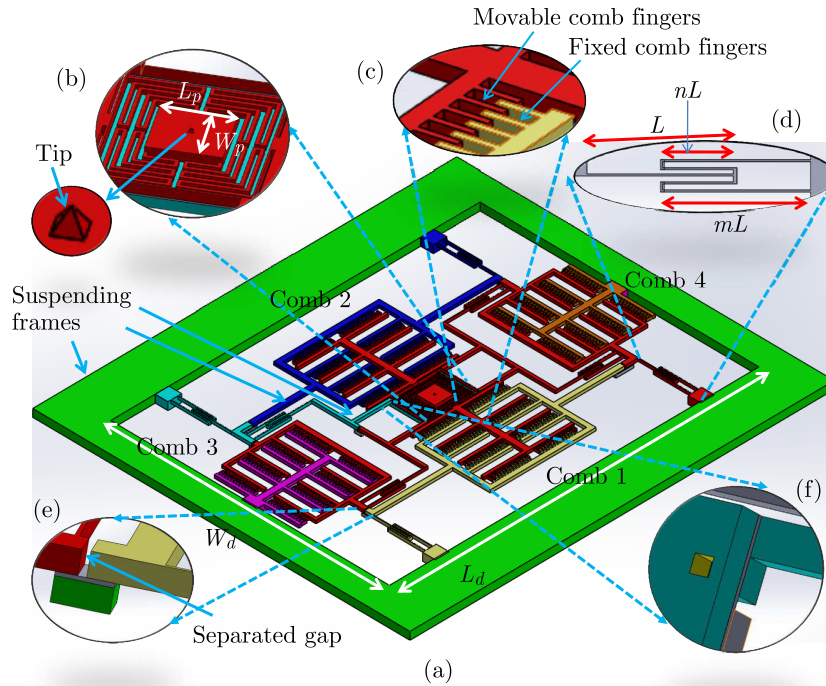
Fig. 1. Three-dimensional schematic view of the xyz micro-actuator (a) and magnified images of interdigitated comb drives (b), z-axis actuator (c), folded springs (d), mechanically coupled but electrically isolated bridge (e), and contact hole for electrically interconnecting between conductive lines on the upper layer and under electrode (back-side counter electrode) (f)
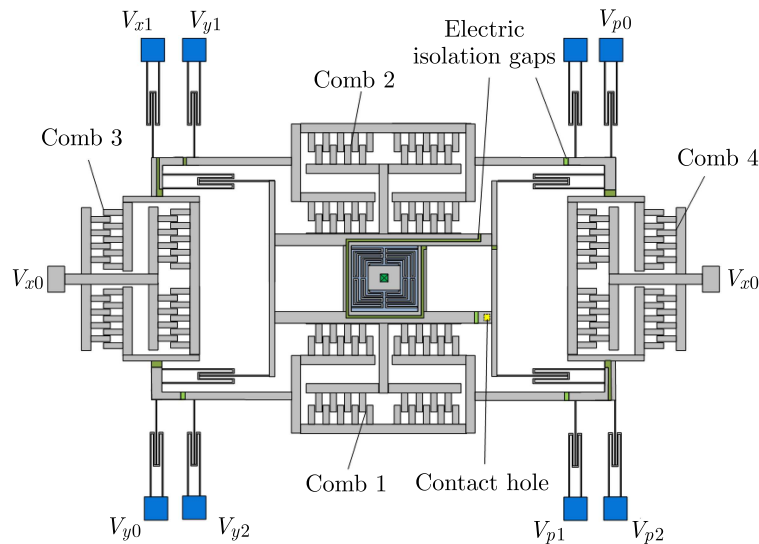
Fig. 2. Diagram of electric interconnection for driving the xyz micro-actuator independently

into eight folded beam springs. Electrodes, $V_{x0}(V_{y0})$, $V_{x1}(V_{y1})$ and $V_{x2}(V_{y2})$ are for driving the center plate along the $x(y)$ axis while two electrodes, V_{p0} and V_{p1} are for supplying voltage for the z-axis actuation. Using the three driving electrodes for the x and y actuator, we can use a differential driving mechanism to enhance the x and y displacements and the linear dependence between the controlling voltage and the displacements (Chu *et al.*, 2011).

3.   Analysis model

To investigate the operation characteristics of the xyz micro-actuator, calculation and numerical methods are used, and several assumptions for simplifying the calculations are given. The micro--actuator is asumed to be made of single crystal silicon. The assumptions of the kinematic theory conform to the Bernoulli-Euler beam theory. The properties of the air operation medium and single crystal silicon are shown in Table 1. In the following, we will present models for investigating the operation characteristics of the micro-actuator.

Table 1. Physical properties of the air operation medium and single crystal silicon

Properties	Air	Silicon
Density [kg/m^3]	1.2	2329
Elastic modulus [N/m^2]		$170 \cdot 10^9$
Poisson ratio		0.28
Dielectric constant	1	11.68
Viscous [Ns/m^2]	$1.8 \cdot 10^{-5}$	

3.1.   The z-axis actuator

As presented in Fig. 1, the xyz micro-actuator uses a parallel-plate capacitive actuator for controlling the z-axis displacement of the probe. The center plate of the z-axis actuator is connected to the xy actuator by four extended crab-leg beam springs. The counter electrode is designed at the backside of the center plate for forming a parallel-plate capacitive actuation. To investigate the operation of this actuator, a single degree of freedom mass-spring system model is used. The movable part consists of the center plate, four springs having the effective mass m_{eq} and a damper. The four spring system has the effective stiffness k_z. The damper is to describe damped vibration caused by the squeeze film air damping effect (Chu, 2016; Bao, 2005). The resonant angular frequency of this actuator ω_z is found from

$$\omega_z = \sqrt{\frac{k_z}{M_z}} \tag{3.1}$$

in which M_z is the sum of the effective mass m_{eq} and mass of the center plate. $m_{eq}(= 13m_b/35)$ is the equivalent mass of the beam derived by the Rayleigh method (Gere and Timoshenko, 1997), in which m_b is mass of the beam.

The extended crab-leg beam spring is shown in Fig. 3a. For convenience, in deriving the expression of the stiffness, we interporate the spring unit as in Fig. 3b. We can divide the spring into three parts, fixed-guided beams with lengths l_a and l_b, and three crab-leg spring units with lengths (l_{c11}, l_{c12}), (l_{c21}, l_{c22}), and (l_{c31}, l_{c32}). The stiffness of the fixed-guided beams $l_{a,b}$ is

$$K_{a,b} = \frac{Ew_{cs}t_z^3}{4l_{a,b}^3} \tag{3.2}$$

where w_{cs} and t_z are width and thickness of the extended crab-leg beam spring.

The stiffness of the crab-leg spring unit is calculated by (Beer $et\ al.$, 2003; Liu, 2011)

$$K_c = \frac{1}{\frac{(l_1-K_2)^2 l_2}{GI_p} + \frac{l_1^3+l_2^3+3K_2 l_1(K_2-l_1)}{3EI_1}} \tag{3.3}$$

where l_1 and l_2 are lengths of the crab-leg beam unit, Fig. 3b, and

$$K_2 = -\frac{K_{2P}}{\delta_{2P}} \qquad\qquad K_{2P} = \frac{l_1^2}{2EI_1} - \frac{l_1 l_2}{GI_P} \qquad\qquad \delta_{2P} = \frac{l_1}{EI_1} - \frac{l_2}{GI_P} \tag{3.4}$$
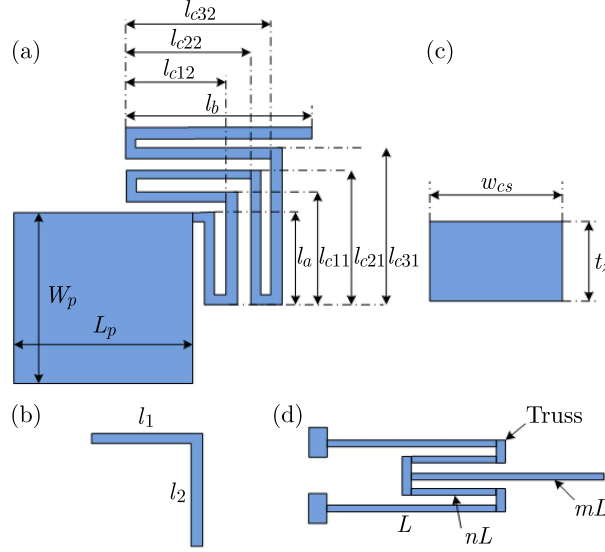
Fig. 3. Schematic drawing of springs: (a) extended crab-leg beams spring for the z-axis actuator, (b) simplified crab-leg spring unit with defined dimensions and (c) folded beam spring for the xy actuator

Here I_P is the polar moment of inertia of the cross-sectional area of the crab-leg beam given by

$$I_P = \frac{1}{16}\Big[w_{cs}t_z^3\Big(\frac{16}{3} - 3.36\frac{t_z}{w_{cs}}\Big)\Big] \tag{3.5}$$

where $G(= E/[2(1 + \nu)])$ is shear modulus in which ν is Poisson's ratio of silicon, and $I_1(= w_{cs}t_z^3/12)$ is the inertial moment of the cross-section about its neutral axis.

Thus, the total stiffness of the extended crab-leg beam spring can be calculated by

$$k_z = \frac{1}{\frac{1}{K_a} + \frac{1}{K_{c1}} + \frac{1}{K_{c2}} + \frac{1}{K_{c3}} + \frac{1}{K_b}} \tag{3.6}$$

Here, K_{c1}, K_{c2}, and K_{c3} are stiffnesses of the three crab-leg beam units, Fig. 3a, which are found from Eq. (3.3).

The electrostatic force acting on the center plate (the movable electrode) is evaluated by

$$F_{ele} = -\frac{1}{2}\varepsilon_o\frac{V^2 A}{(g_z - d_z)^2} \tag{3.7}$$

where A is the electrode overlap area, V is the applied voltage, g_z is the gap between two electrodes and d_z is the vertical displacement. The displacement of the movable electrode can be controlled by applying voltage to the actuation electrodes. The minus means that the electrostatic force is always an attractive force. Under a DC driving condition, the displacement d_z along the z-axis can be derived based on the balance between the electrostatic force and the elastic force as follows

$$k_z d_z = \frac{1}{2}\varepsilon_o\frac{V_{dc}^2 A}{(g_z - d_z)^2} \tag{3.8}$$

To solve this equation, we can use a numerical method.

In the parallel-plate actuation, there is a static equilibrium position ($V_{ac} = 0$) where the electrostatic force balances with the elastic force. The DC applied voltage at this critical state is called to be $V_{pull-in}$ at $d_z = g_z/3$ (Bao and Yang, 2007)

$$V_{pull-in} = \sqrt{\frac{8}{27}\frac{k_z g_z^3}{\varepsilon_o A}} \tag{3.9}$$

when V_{dc} is larger than or equal to $V_{pull-in}$, the equilibrium position does not exist, the probe will be at an unstable state and can contact or snap with the counter electrode. So, for the electrostatic actuator used in the scanning probe, the operating voltage of the actuator must be smaller than $V_{pull-in}$.

3.2. The xy actuators

The displacement along the x and y axes is drived by interdigitated comb drives (Fig. 1). The movable combs are suspended on the folded beam springs with stiffness $k_{x,y}$. The displacement of the center plate along the x and y axes actuated by the lateral force $F_l(= n_c \varepsilon_o t V^2 / g_c)$ is calculated by (Legtenberg et $al.$, 1996)

$$x, y = \frac{2n_c \varepsilon_o t_{xy}}{k_{x,y} g_c} V_{dc}^2 \tag{3.10}$$

where n_c is the number of the comb fingers, t_{xy} is thickness of the comb fingers, $x(y)$ is the displacement of the center plate along the $x(y)$ axis, g_c is the gap between two adjacent fingers. In investigations, t_{xy} is equal to thickness t of the xyz micro-actuator, while t_z can be different from t_{xy}. This choice is dependent on design requirements of the device.

As presented, the folded beam spring is used for suspending the frames moving in the x and y axes. In this study, the folded beam springs in the two axes are identical. The stiffness of the folded beam spring in the x and y direction is derived based on the stiffness of folded-beam spring components connected in series and parallel as

$$k_{x,y} = \frac{2Ew_{fb}^3 t_{xy}}{(1 + 2m^3 + n^3)L^3} \tag{3.11}$$

where m and n are multiples of L showing length of the folded-beam spring components as shown in Fig. 3d. In this study, $m = 1$ and $n = 0.5$. The dimensional parameters of the plate, springs and comb fingers are shown in Table 2.

Table 2. Dimensional parameters of the xyz micro-actuator

Structures	Length [μm]	Width [μm]	Height [μm]
Plate ($L_p \times W_p \times t$)	200	200	30
Tip ($_L t \times W_t \times h_t$)	14	14	10
Comb finger ($L_c \times W_c \times t$)	100	5	10-30
Beam L ($L_L \times W_L \times t$)	100-600	5-15	10-30
Total size of device ($L_d \times W_d \times t$)	4210	5060	10-30

3.3. Air damping in the xyz micro-actuator

In the xyz micro-actuator, there are two types of air damping, which depend on relative motion between structure components. When the structure components move perpendicularly to each other, squeeze film air damping is taken into consideration. This case is corresponding to the z-axis actuator. When the gap between two actuation electrodes of the z-axis actuator is small, the squeeze film air damping is a dominant energy dissipation mechanism in the xyz micro-actuator. The damping ratio of the z-axis actuator ζ_z is given by (Bao, 2005)

$$\zeta_z = \frac{\mu w_p^4}{0.84 m_{eq} g^3 \omega_z} \tag{3.12}$$

where ω_z is the angular frequency of the z-axis actuator, w_p is width of the movable electrode (the center plate), m_{eq} is the equivalent mass of the actuator, $\mu_0(= 18.5 \cdot 10^{-5}\,\mathrm{Pa\,s})$ is the viscosity coefficient of the air. For low pressure, the effective viscosity coefficient is used (Veijola *et al.*, 1998)

$$\mu_{eff} = \frac{\mu_0}{1 + 9.658 K_n^{1.159}} \tag{3.13}$$

where K_n is the Knudsen number calculated by (Chu and Hane, 2011)

$$K_n = \frac{\lambda}{d_a} \tag{3.14}$$

Here λ is the mean-free path and d_a is the typical dimension of the device. The mean-free path is given by $\lambda = kT/(\sqrt{2}\pi P d^2)$ where $k(= 1.38 \cdot 10^{-23}\,\mathrm{J/K})$ is the Boltzman constant, T is air temperature, P is air pressure, and $d(= 4.19 \cdot 10^{-10}\,\mathrm{m})$ is the collision diameter of gas molecules.

The remaining case is when the structure components are parallelly moving to each other, which corresponds to slide motion of the comb drives in the xy actuators. In this case, slide film air damping is considered. The damping ratio $\zeta_{x,y}$ is calculated for motion in the x and y directions as follows

$$\zeta_{(x,y)} = \frac{\mu A_s}{2d\sqrt{m_{eff}^{x,y} k_{x,y}}} \tag{3.15}$$

where A_s is the area of sidewalls of the overlap, and $m_{eff}^{x,y}$ are the effective masses of the actuator along the x and y vibration directions, respectively.

The quality factor of the xyz micro-actuator in the x, y and z directions, $Q_{x,y,z}$ is calculated by (Bao, 2005)

$$Q_{x,y,z} = \frac{1}{2\xi_{x,y,z}} \tag{3.16}$$

Thus, we have built a model for analyzing the operation characteristics of the xyz micro-actuator. In the following, we will present results obtained by employing the above formulated equations. The calculation results are compared to those obtained from numerical simulation using Comsol Multiphysics 4.3. In this study, the used Comsol module is a MEMS module.

4. Results and discussion

The first three mode shapes and natural frequencies of the extended crab-leg beam spring-based z-axis actuator obtained from simulation are shown in Fig. 4. The parameters of the spring and the center plate are shown in Fig. 4 and Table 2. Here, we fixed the length of the crab-leg beam spring in investigations while changing its width and thickness. The first mode is the operation mode of the z-axis actuator. The natural frequencies of the first and second mode are 25.4 kHz and 44.1 kHz, respectively. The natural frequency discrepancy between the first and second mode is 73.6%, which satisfies the requirement of the low mode cross-talk (Trinh *et al.*, 2013). The stiffness of the spring k_z calculated by Eq. (3.6) is 88.9 N/m. The effective mass of the center plate and the extended crab-leg beams spring M_z is $3.66 \cdot 10^{-9}$ kg. The resonant frequency is calculated by Eq. (3.1) to be 24.8 kHz. The error between the calculation and simulation results is 2.4%. So, the theoretical expressions can be used to optimize the operating frequency of the z-axis actuator.

For integrating the z-axis actuator in the xyz actuator, we further investigate the mode cross-talk, pull-in voltage, and the resonant frequency depending on the width of the spring

(a) Mode 1 (Mode z)   (b) Mode 2   (c) Mode 3

$f_1 = 25.4\,\mathrm{kHz}$ $f_2 = 44.1\,\mathrm{kHz}$ $f_3 = 56.1\,\mathrm{kHz}$
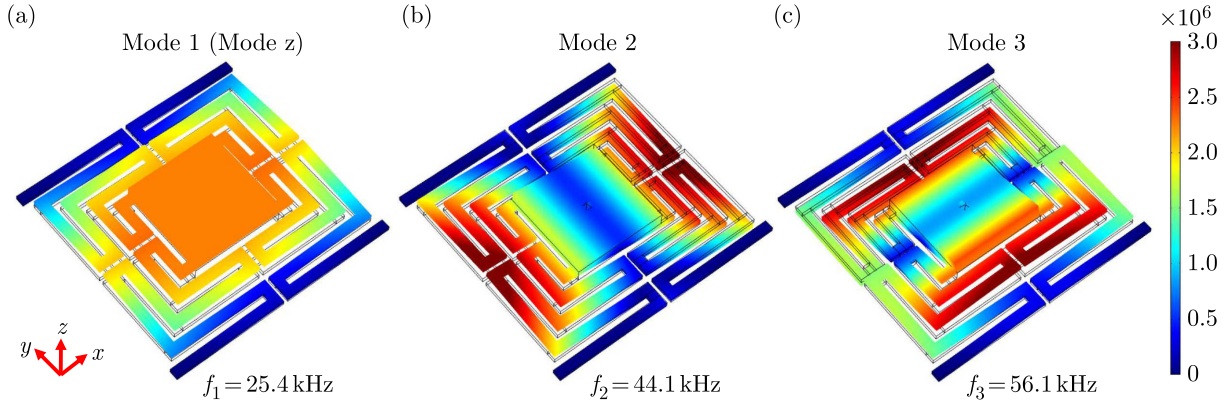
Fig. 4. The first three mode shapes and natural frequencies of the z-axis actuator are shown respectively in (a), (b), and (c). The dimensional parameters of the extended crab-leg beams spring are $l_a = 230\,\mu\mathrm{m}$, $l_b = 95\,\mu\mathrm{m}$, $l_{c11} = 160\,\mu\mathrm{m}$, $l_{c12} = 215\,\mu\mathrm{m}$, $l_{c21} = 145\,\mu\mathrm{m}$, $l_{c22} = 160\,\mu\mathrm{m}$, $l_{c31} = 95\,\mu\mathrm{m}$, $l_{c32} = 145\,\mu\mathrm{m}$, $w_{cs} = 20\,\mu\mathrm{m}$ and $t_z = 10\,\mu\mathrm{m}$
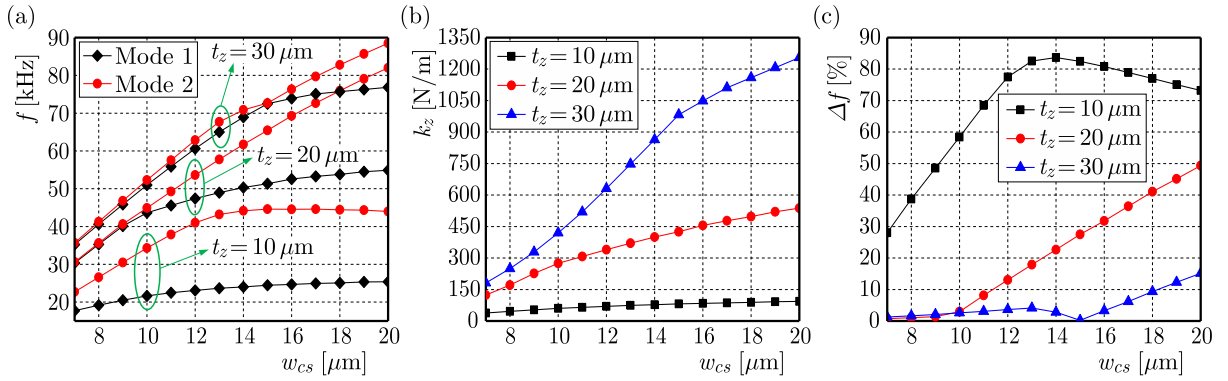
Fig. 5. (a) Frequency of modes 1 and 2, (b) stiffness of mode 1, and (c) frequency discrepancy between modes 1 and 2 of the z actuator investigated as a function of width of extended crab-leg beam spring for three thicknesses of the spring beam, $t_z = 10$, 20 and $30\,\mu\mathrm{m}$

beam for different device layer thicknesses. The frequency of modes 1 and 2, stiffness of mode 1, and frequency discrepancy between modes 1 and 2 of the z-axis actuator investigated as a function of width of the extended crab-leg beam spring for three thicknesses of the spring beam, $t_z = 10\,\mu\mathrm{m}$, $20\,\mu\mathrm{m}$ and $30\,\mu\mathrm{m}$, are shown in Figs. 5a-5c, respectively. To obtain the stiffness k_z of the z-axis actuator (mode 1) as shown in Fig. 5b, a semi-analytical method is used. k_z is determined from the frequency f_z of mode 1 and the effective mass M_z by $k_z = (2\pi f_z)^2 M_z$. Thus, the operation frequency of the z-axis actuator increases with width of the spring beam. For thinner spring beams, f_z is lower and has a narrower variation range of the operation frequency compared to that of thicker spring beams, Fig. 5a. For example, at $t_z = 10\,\mu\mathrm{m}$, f_z is only modified by 40%, from 17.7 kHz to 25.4 kHz, while at $t_z = 30\,\mu\mathrm{m}$, f_z is varied up to 118%, from 35.3 kHz to 76.9 kHz. The variation range of the operation frequency is chosen based on different applications. However, for thicker spring beams the frequency discrepancy δf becomes smaller (Fig. 5c), which leads to the increment of the mode coupling in the z-axis actuator, meaning that the mode cross-talk is high. This can be explained that when thickness of the spring beam increases, the flexural modes in the plane become prior to the flexural mode in the z-direction. In general, to satisfy the requirement of the low mode cross-talk, the aspect ratio, w_{cs}/t_z, must be large enough. For example, at $t_z = 10\,\mu\mathrm{m}$, to obtain δf larger than 40%, w_{cs}/t_z must be larger than 0.8, while at $t_z = 20\,\mu\mathrm{m}$, w_{cs}/t_z must be larger than 0.87. In this study, we have kept the length of total spring beams to maintain the footprint of the device

(Table 2) while its admired operation characteristics can be well modified by varying width and thickness of the spring beams.

The pull-in voltage $V_{pull-in}$ is investigated as a function of the beam width for three thickness values, $t_z = 10\,\mu\text{m}$, $20\,\mu\text{m}$ and $30\,\mu\text{m}$, as shown in Fig. 6. The parameters range chosen for investigation is based on the criterion of practice fabrication that the width/thickness to length aspect ratio of the beam is less than 20. Thus, when the beam width increases, $V_{pull-in}$ increases monotonically with w_{cs}. From these investigations, we can choose the applied voltage suitable for the z-axis actuator to avoid the sticking effect in the operation.
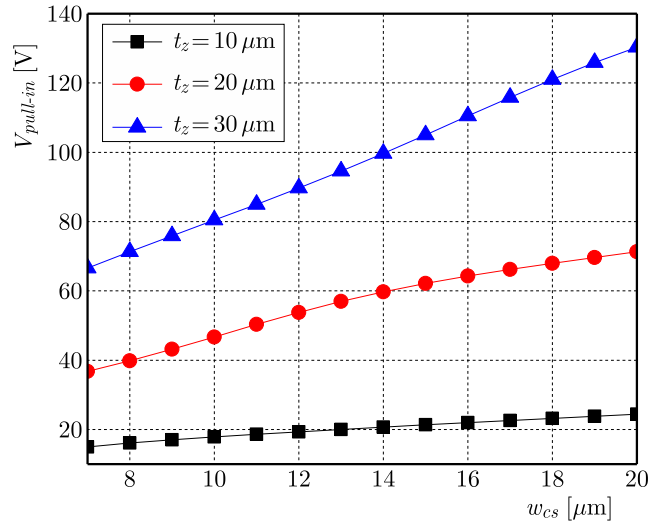
Fig. 6. Pull-in voltage of the z-axis actuator as a function of width of the extended crab-leg beam spring with the actuation gap, $g_z = 3\,\mu\text{m}$, for three different thicknesses $t_z = 10\,\mu\text{m}$, $20\,\mu\text{m}$ and $30\,\mu\text{m}$

The mode shapes and natural frequencies of three operation modes of the xyz micro-actuator are shown in Fig. 7. The two first modes are in-plane vibration modes in the x and y directions having the frequencies f_x and f_y, respectively. The remaining mode is the out-of-plane vibration mode (the z-axis mode) having the frequency f_z. The resonant frequency values in the three vibration directions theoretically calculated using Eqs. (3.1), (3.6) and (3.11) are also shown in Table 3. The errors between the calculated and simulated results for f_x, f_y, and f_z are 2.9%, 7.2% and 2.3%, respectively. To independently drive the micro-actuator along the x, y and z axes, the mode split has to be large enough to suppress the mode coupling (Trinh *et al.*, 2013; Weinberg and Kourepenis, 2006; Fang *et al.*, 2018, Acar and Shkel, 2009). The mode split between the first and second modes is 88.23%, while these two modes are completely splitted with the third mode (0.85 kHz and 1.6 kHz compared to 27.9 kHz). The operation frequencies and mode splits in the proposed xyz micro-actuator are easily controlled by varying stiffness of the springs.

Table 3. Analytical and simulation results of natural frequencies of the xyz micro-actuator

	f_x [kHz]	f_y [kHz]	f_z [kHz]
Theoretical analysis	0.87	1.51	24.82
FEM	0.85	1.62	25.41
Δ [%]	2.9	-7.2	2.3

We have also investigated the resonant operation frequency of the three interested modes depending on the thickness to width aspect ratios of the spring beams, $t/w_{cs,fb}$, as shown in Fig. 8. The frequencies of the x and y in-plane modes are almost independent of the thickness t_{xy}. However, the frequency of the out-of-plane mode is dependent on the aspect ratio of t_z/w_{cs}. The frequency is linearly proportional to t_z/w_{cs}. To meet the operation requirement with the low
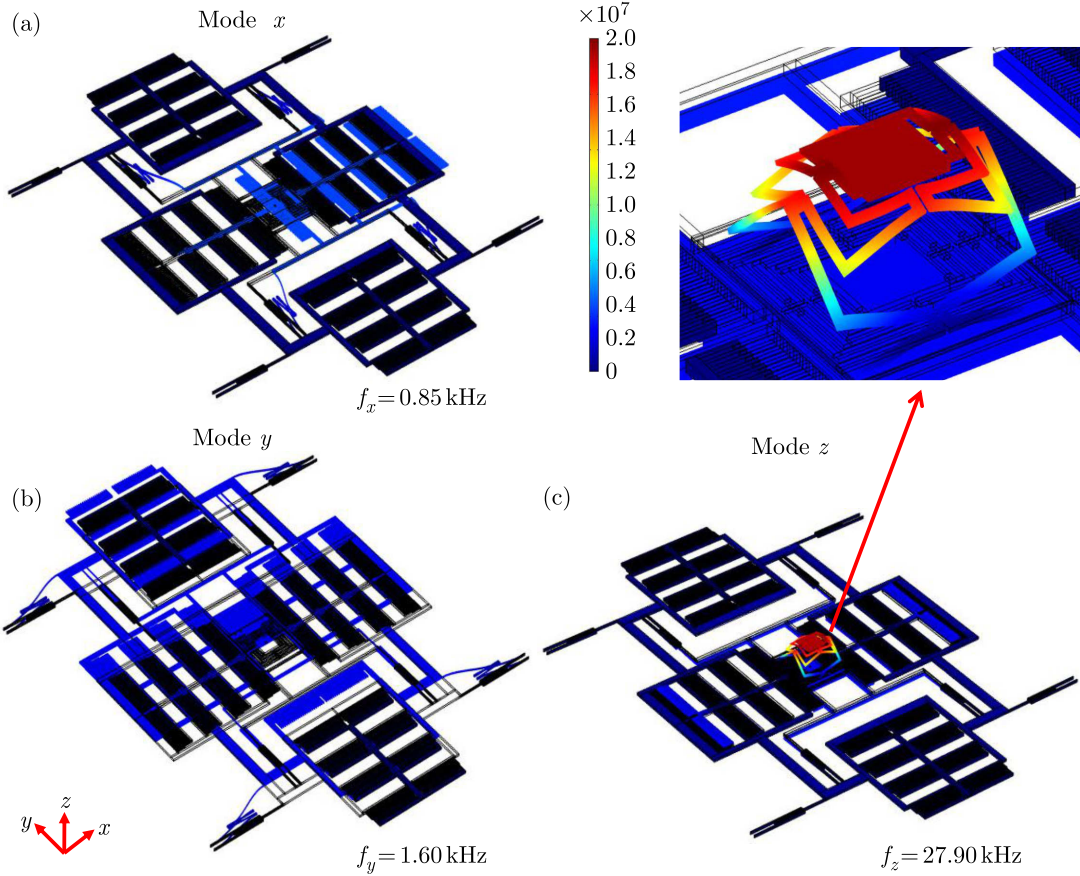
Fig. 7. The first three mode shapes and natural frequencies of the xyz micro-actuator are shown in (a), (b), and (c), respectively. The dimensional parameters are shown in Table 2, in which $L = 600\,\mu$m, $t_{xy} = 30\,\mu$m, $t_z = 10\,\mu$m, $w_{fb} = 5\,\mu$m, and $w_{cs} = 20\,\mu$m. The inset on the right corner shows a magnified image of the z mode of the z-axis actuator integrated in the xyz micro-actuator
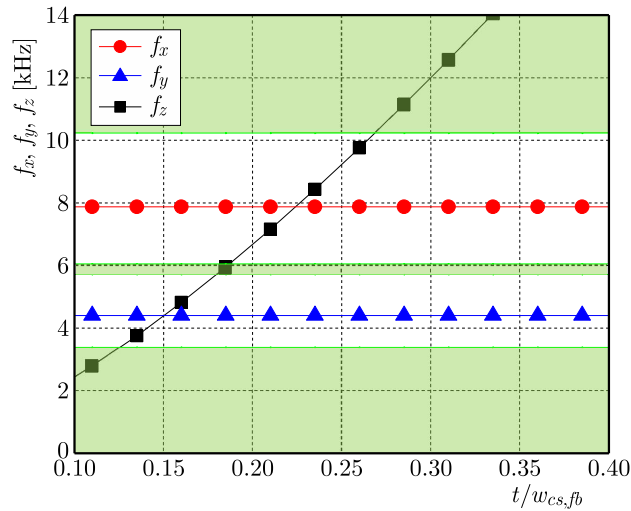
Fig. 8. The frequency of the out-of-plane mode versus the aspect ratio of $t/w_{cs,fb}$, here, $t = t_z = t_{xy}$

mode cross-talk ($\delta f > 30\%$) (Trinh $et~al.$, 2013; Weinberg and Kourepenis, 2006; Acar and Shkel, 2009), the operation frequency f_z can be designed within $[f_x, f_y]$ or outside this range, as shown in green strips in Fig. 8, by modifying the parameters of the extended crab-leg beam spring as in the design of the z-axis actuator. The mode split between the x and y axes is defined

by appropriately choosing the parameters of the folded beam spring. For example, to satisfy $\delta f > 30\%$, the ratio t_z/w_{cs} must be > 0.27, < 0.13 or within $[0.8, 0.9]$. In this study, the folded beam springs along the x and y axes are identical. The frequency discrepancy between f_x and f_y are generated from the difference in the effective mass between the x and y in-plane modes. To modify discrepancy in this frequency, we can choose different design parameters of the folded beam springs along the x and y axes.

To choose the desired operation frequency of the xy actuator, we have investigated the dependence of the frequencies f_x and f_y and the stiffnesses k_x and k_y of the xyz actuator on the width w_{fb} of the spring beams, see Fig. 9a and 9b for three thicknesses of the spring beams, $t_{xy} = 10\,\mu\text{m}$, $20\,\mu\text{m}$ and $30\,\mu\text{m}$. Figures 9c and 9d show the frequencies f_x and f_y and the stiffnesses k_x and k_y of the xyz actuator depending on the length L for three widths of the spring beam, $w_{fb} = 5\,\mu\text{m}$, $7\,\mu\text{m}$, and $10\,\mu\text{m}$.
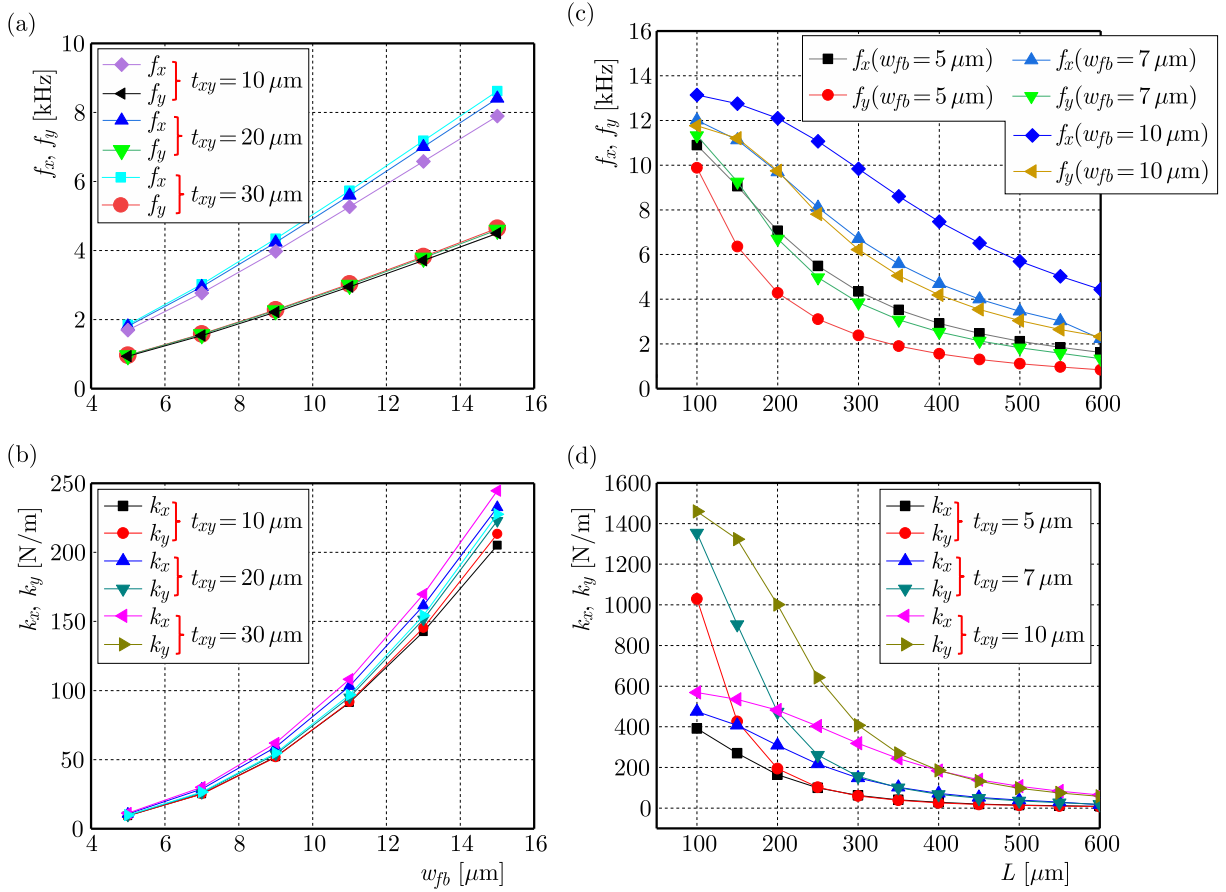
Fig. 9. Dependence of the frequencies f_x and f_y and the stiffnesses k_x and k_y of the xyz actuator on the width w_{fb} and length L of the folded spring beam, respectively, for: (a), (b) $t_{xy} = 10\,\mu\text{m}$, $20\,\mu\text{m}$ and $30\,\mu\text{m}$ and (c), (d) $w_{fb} = 5\,\mu\text{m}$, $7\,\mu\text{m}$ and $10\,\mu\text{m}$

Thus, we can choose a wide range of the operation frequency for both f_x and f_y. In the investigated L and w range, f_x and f_y can be varied from $1.625\,\text{kHz}$ to $13.141\,\text{kHz}$ and from $0.847\,\text{kHz}$ to $11.766\,\text{kHz}$, respectively.

The displacements of the center plate along the x, y and z axes are investigated as a function of applied voltage for three different gaps between the two adjacent fingers, $g_c = 1\,\mu\text{m}$, $1.5\,\mu\text{m}$ and $2\,\mu\text{m}$ and three actuation gaps, $g_z = 2\,\mu\text{m}$, $3\,\mu\text{m}$ and $4\,\mu\text{m}$ by using Eq. (3.10) and Eq. (3.8), as shown in Fig. 10a and 10b, respectively. The number of comb finger pairs in each comb drive is 160. For the gap between comb fingers of $1\,\mu\text{m}$, the displacement of the plate along the x and y axes is $57\,\mu\text{m}$ for the applied voltage of $60\,\text{V}$. For the z-axis actuator, the fixed

electrode area is equal to the entire back-side area of the center plate. The gap between the two actuation electrodes is $3\,\mu$m. The maximum displacement of the center plate in this direction is $1\,\mu$m with respect to the pull-in voltage of $33.8\,$V by Eq. (3.9), which is in good agreement with that obtained from simulation for $34\,$V.
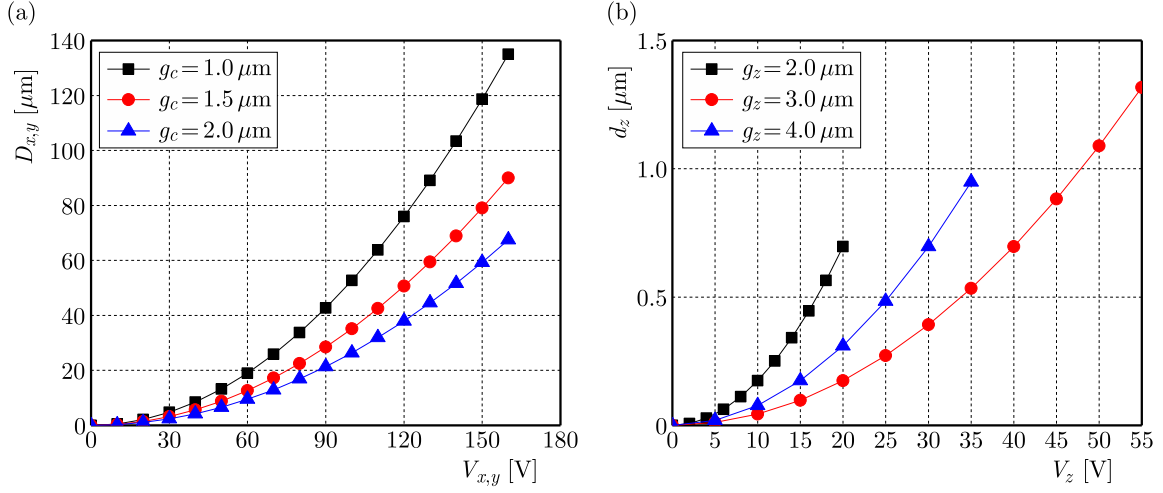
Fig. 10. The x and y displacements of the center plate are investigated as a function of applied voltage for three different gaps between two adjacent fingers, $g_c = 1\,\mu$m, $1.5\,\mu$m and $2\,\mu$m with $t_{xy} = 30\,\mu$m (a) and the z displacement of the center plate is investigated as a function of applied voltage for three actuation gaps, $g_z = 2\,\mu$m, $3\,\mu$m and $4\,\mu$m with $t_z = 10\,\mu$m
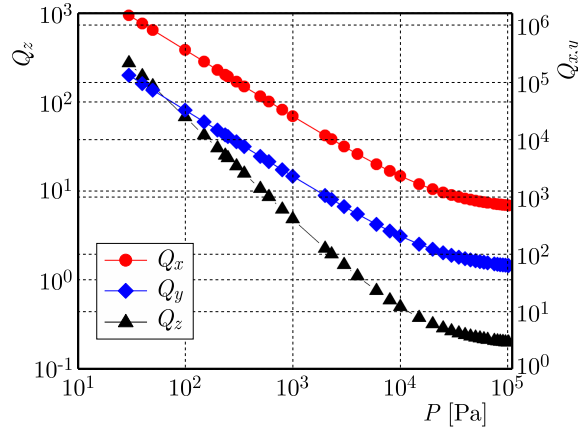
Fig. 11. Quality factors of the xyz micro-actuator, $Q_{x,y,z}$, investigated as a function of ambient pressure for three vibration directions, the x and y axes (slide film air damping) and the z-axis (squeeze film air damping)

The quality factors of the xyz actuator depending on ambient pressure are shown in Fig. 11. As seen in Fig. 11, the quality factor in the z-axis direction is lower than that compared in the x and y directions. This also means that damping in the z-axis is larger than that compared to the two remaining axes. When the ambient pressure is higher than $10^4\,$Pa, Q is almost indepedent of P. For dynamic driving of the actuator, the vibration amplitue of the micro-actuator in each direction is calcualted by $Z = \chi Q$, in which χ is a constant depending on the dimensional parameters of the micro-actuator and the driving electrostatic force (Chu and Hane, 2011). Under the atmospheric air condition, $Q_{x,y,z}$ are calculated to be 717.4, 64.7 and 0.2, respectively. However, at a vacuum condition of about $10^3\,$Pa, the quality factors $Q_{x,y,z}$ of the xyz micro-actuator vibrating in the x, y and z axes are $25.7 \cdot 10^3$, 2.3×10^3 and 4.87, respectively. Therefore, if the xyz micro-actuator operates under this resonant condition, the

vibration amplitudes along the x, y and z axes are amplified by 35.82, 35.5 and 24.4 times, respectively.

5. Conclusion

We have presented design and simulation of an xyz micro-actuator whose displacements can be independently controlled in three orthogonal directions. The independently controlled displacement is achieved by designing a center plate suspended by a spring system that is only compliant to the z displacement. This whole plate system is suspended on a xy actuator. The independent control in the three orthogonal directions is carried out by routing conductive lines along the springs and using a silicon-on-insulator wafer feed-through technique and electric isolation trenches. The optimal design of the micro-actuator is carried out by an established analysis model based on solid and fluidic mechanical theory as well as electrostatic theory. The analytical results are in good agreement with simulation results using the finite element method. The investigated results show that we can control independently the xyz micro-actuator in the three orthogonal directions with a suppressed mode cross-talk. The displacements in the x and y directions can reach $57\,\mu$m at a moderate applied voltage of $60\,$V. The displacement in the z direction can achieve $1\,\mu$m at an applied voltage of $33.8\,$V. The operation voltages of the device can be further reduced by operating it in vacuum.

References

1. ACAR C., SHKEL A., 2009, *MEMS Vibratory Gyroscopes Structural Approaches to Improve Robustness*, Springer Science & Business Media LLC, USA

2. ANDO Y., 2004, Development of three-dimensional electrostatic stages for scanning probe microscope, *Sensors and Actuators A: Physical*, **114**, 2-3, 285-291

3. BAO M., 2005, *Analysis and Design Principles of MEMS Devices*, 1st ed., Amsterdam: Elsevier B.V.

4. BAO M., YANG H., 2007, Squeeze film air damping in MEMS, *Sensors and Actuators A: Physical*, **136**, 3-27

5. BEER F.P., JOHNSTON E.R., DE WOLF J.T., 2003, *Mechanics of Materials*, Tsinghua University Press, China

6. CHU H.M., 2016, Air damping models for micro- and nano-mechanical beam resonators in molecular-flow regime, *Vacuum*, **126**, 45-50

7. CHU H.M., HANE K., 2011, Design, fabrication and vacuum operation characteristics of two--dimensional comb-drive micro-scanner, *Sensors and Actuators A: Physical*, **165**, 422-430

8. CHU H.M., MIZUNO J., HANE K., TAKAGI T., 2011, Compact slanted comb two-axis micro--mirror scanner fabricated by silicon-on-insulator micromachining, *Journal of Vacuum Science and Technology*, **B 29**, 042001

9. CORREA J., KOO B., FERREIRA P., 2016, Parallel-kinematics XYZ MEMS. Part 1: Kinematics and design for fabrication, *Precision Engineering*, **46**, 135-146

10. DONG J., FERREIRA P.M., 2009, Electrostatically actuated cantilever with SOI-MEMS parallel kinematic XY stage, *Journal of Microelectromechanical Systems*, **18**, 641-651

11. GERE J.M., TIMOSHENKO S.P., 1997, *Mechanics of Materials*, PWS Publishing Company

12. HU H., KIM H., SOMNATH S., 2017, Tip-based nanofabrication for scalable manufacturing, *Micromachines*, **8**, 3, 90

13. HUO F., ZHENG G., LIAO X., GIAM L.R., CHAI J., CHEN X., SHIM W., MIRKIN C.A., 2010, Beam pen lithography, *Nature Nanotechnology*, **5**, 637-640

14. KIM Y.S., DAGALAKIS N.G., GUPTA S.K., 2014, Design of MEMS based three-axis motion stage by incorporating a nested structure, *Journal of Micromechanics and Microengineering*, **24**, 7, 075009

15. LEGTENBERG R., GROENEVELD A.W., ELWENSPOEK M., 1996, Comb-drive actuators for large displacements, *Journal of Micromechanics and Microengineering*, **6**, 3, 320-329

16. LIU X., KIM K., SUN Y., 2007, A MEMS stage for 3-axis nanopositioning, *Journal of Micromechanics and Microengineering*, **17**, 9, 1796-1802

17. LIU Y., 2011, Stiffness calculation of the microstructure with crab-leg flexural suspension, *Advanced Materials Research*, **317-319**, 1123-1126

18. SASAKI M., BONO F., HANE K., 2008, Large-displacement micro-XY-stage with paired moving plates, *Japanese Journal of Applied Physics*, **47**, 4S, 3226

19. TAKAHASHI K., MITA M., FUJITA H., TOSHIYOSHI H., 2009, Switched-layer design for SOI bulk micromachined XYZ stage using stiction bar for interlayer electrical connection, *Journal of Microelectromechanical Systems*, **18**, 4, 818-827

20. TRINH T.Q., NGUYEN L.Q., DAO D.V., CHU H.M., VU H.N., 2013, Design and analysis of a *z*-axis tuning fork gyroscope with guided-mechanical coupling, *Microsystem Technologies*, **20**, 2, 281-289

21. VEIJOLA T., KUISMA H., LAHDENPERÄ J., RYHÄNEN T., 1998, Equivalent-circuit model of the squeezed gas film in a silicon accelerometer, *Sensors and Actuators A: Physical*, **48**, 239-248

22. WANG X., BULLEN D.A., ZOU J., LIU C., MIRKIN C.A., 2004, Thermally actuated probe array for parallel dip-pen nanolithography, *Journal of Vacuum Science and Technology*, **B 22**, 6, 2563-2567

23. WEINBERG M,S., KOUREPENIS A., 2006, Error sources in in-plane silicon tuning-fork MEMS gyroscopes, *Journal of Microelectromechanical Systems*, **15**, 3, 479-491

24. XU H., ONO T., ZHANG D.Y., ESASHI M., 2006, Fabrication and characterizations of a monolithic PZT microstage, *Microsystem Technologies*, **12**, 9, 883-890

25. ZHANG W.M., YAN H., PENG Z.K., MENG G., 2014, Electrostatic pull-in instability in MEMS/NEMS: A review, *Sensors and Actuators A: Physical*, **214**, 187-218